PCCP

ROYAL SOCIETY OF CHEMISTRY

PAPER

View Article Online
View Journal | View Issue

Cite this: *Phys. Chem. Chem. Phys.*, 2025, **27**, 8098

Additive-assisted oriented growth of cobalt oxide: controlled morphology and enhanced supercapacitor performance†

Radhika S. Desai, [ag] Vinayak S. Jadhav, [a] Sidharth R. Pardeshi,[b] Pramod S. Patil, [cd] Mohammad Rafe Hatshan,[e] Yedluri Anil Kumar [f] and Dhanaji S. Dalavi *[a]

This research investigates the supercapacitor properties of cobalt oxide (Co_3O_4) thin films enhanced by five different additives: urea, ammonium chloride (NH_4Cl), ammonium hydroxide (NH_4OH), ammonium fluoride (NH_4F), and hexamethylenetetramine (HMT). The thin films are synthesized using a double hydrothermal approach on stainless steel substrates. Morphological and XRD analyses reveal well-separated Co_3O_4 nanowires stacked together, with diameters ranging from 10 to 34 nm and an average crystallite size between 19 and 23 nm. The additives serve as complexing agents, influencing the pH of the solution and facilitating the formation of cobalt-containing complexes, thereby promoting the uniform growth of Co_3O_4. Notably, the C-HMT nanowires exhibit superior supercapacitive performance, achieving a specific capacitance of 468.68 F g^{-1} at a scan rate of 5 mV s^{-1} and an impressive retention rate of 98.31% after 10 000 cycles at a scan rate of 100 mV s^{-1}. Additionally, a symmetric device composed of two C-HMT electrodes is developed, demonstrating practical application by effectively illuminating five parallel-connected LEDs for approximately 20 seconds. In conclusion, this study presents a pioneering application of C-HMT as a symmetric supercapacitor, showcasing significant advancements in performance for future flexible energy storage devices.

Received 9th October 2024,
Accepted 13th March 2025

DOI: 10.1039/d4cp03874f

rsc.li/pccp

1. Introduction

Spinel-structured cobalt(II,III) oxide, or Co_3O_4, is a promising transition metal oxide (TMO) with considerable potential in energy storage applications. This cost-effective material has gained attention for several key attributes. Co_3O_4 exhibits a high theoretical capacitance (3560 F g^{-1}), undergoing multiple redox reactions involving both cobalt(II) and cobalt(III) states, resulting in a superior capacity compared to other TMOs.[1] With reasonable electrical conductivity (in the range of 10^{-4} to 10^{-2} S cm^{-1}), it facilitates the efficient transport of electrons during charge and discharge cycles.[2] The material often displays pseudocapacitive behaviour, implying that the charge storage mechanism involves faradaic redox reactions at the surface.

Moreover, it exhibits good chemical stability, a crucial factor for long-term cycling stability in energy storage devices, which is pivotal in maintaining electrode performance over numerous charge–discharge cycles. Despite the promising properties of Co_3O_4, it suffers from volume expansion during repetitive charge–discharge cycles. So far, various research groups have studied Co_3O_4 in energy storage applications, employing diverse synthesis techniques and utilizing various transparent conductive electrodes to optimize its performance, often focusing on achieving unique morphologies.[3,4]

However, significant differences emerge when comparing the results of Co_3O_4 deposition on a steel substrate with those on other substrates like nickel foam, carbon fiber cloth (CFC), Ti substrates, *etc.* It is commonly observed that a Co_3O_4 electrode on nickel foam results in a higher capacitance than on steel substrates. For instance, Pan *et al.* synthesized Co_3O_4 nanosheet electrodes on Ni foam achieving a specific capacitance of 6469 F g^{-1} at a current density of 5 mA cm^{-2}, and the device retained 81.6% of its capacitance after 2000

[a] *Department of Physics, Krishna Mahavidyalaya, Rethare Bk, Post-Shivnagar, Tal-Karad, Dist. Satara 415108, Maharashtra, India. E-mail: dhanuphysics@gmail.com*
[b] *Department of Physics, Mahindra University, Hyderabad, India*
[c] *Department of Physics, Shivaji University, Kolhapur 416004, India*
[d] *National Dong Hwa University, Hualien, Taiwan*
[e] *Department of Chemistry, College of Science, King Saud University, P.O. Box 2455, Riyadh 11451, Saudi Arabia*
[f] *Department of Materials Science and Engineering, Seoul National University of Science and Technology, Seoul 01811, Republic of Korea*
[g] *Shree Santkrupa Institute of Engineering & Technology, Ghogaon, India*

† Electronic supplementary information (ESI) available. See DOI: https://doi.org/10.1039/d4cp03874f

charge–discharge cycles at 15 mA cm^{-2}.[5] Similarly, Kung *et al.* electrodeposited Co_3O_4 nanosheets on a flexible Ti substrate using a one-step potentiostatic method, followed by UV-ozone treatment. This process resulted in a specific capacitance of 1033.3 F g^{-1} at 2.5 A g^{-1} and displayed long-term stability retaining 77% of the specific capacitance after 3000 repeated charge–discharge cycles.[6] In contrast, if we compare this with a steel substrate, Tummala *et al.* deposited nanostructured Co_3O_4 electrodes directly on a flexible steel sheet and a specific capacitance of approximately 162 F g^{-1} with a retention of capacity of 72.2% after 1000 cycles was observed at a specific current rate of 2.75 A g^{-1}.[7] Additionally, Jagadale *et al.*[8] and Khavale *et al.*[9] successfully prepared Co_3O_4 *via* the potentiodynamic electrodeposition method on a stainless steel substrate with a specific capacitance of 365 F g^{-1} at the scan rate of 5 mV s^{-1} and 441.17 F g^{-1} at a scan rate of 2 mV s^{-1} in 1 M KOH, respectively. Furthermore, Gaikar *et al.* found that the nano-grass-type Co_3O_4 electrode exhibited a higher specific capacity of 66.40 mA h g^{-1} at 1 mA cm^{-2} current density and retained approximately 90% capacity after 1000 cycles.[10] Additionally, Gavande *et al.* synthesized Co_3O_4 electrodes by potentiostatic[11] and chronoamperometry[12] methods, achieving a specific capacitance of 284.4 F g^{-1} and 294.67 F g^{-1} at a scan rate of 5 mV s^{-1} in 1 M aqueous Na_2SO_4 electrolyte, respectively. Wang *et al.* investigated the supercapacitance properties of nanoporous Co_3O_4 nanorods. The grown Co_3O_4 achieved a BET_{SSA} of about 232 m^2 g^{-1}. The high BET_{SSA} and nanoporous cobalt oxide nanorod (with a diameter of 400 nm) morphology resulted in a high specific capacitance (C_s) of 281 F g^{-1} in an aqueous electrolyte.[13] Cui *et al.* used cetyltrimethylammonium bromide (CTAB) as a soft template (cationic surfactant), contributing to consistent morphology growth with an ordered chain structure. The reported Co_3O_4 nanorods (diameter 20–50 nm) maintained their initial C_s (456 F g^{-1}) even after 500 cycles without any significant loss.[14] Nakhanivej *et al.* reported that two-dimensional black phosphorus nanosheets demonstrate a remarkable capacitance of 478 F g^{-1}, significantly outperforming bulk black phosphorus by a factor of four. These nanosheets exhibited an impressive rate capability of approximately 72%, compared to only 21.2% for black phosphorus, and maintained around 91% capacity retention after 50 000 charge–discharge cycles.[15] Wang *et al.* reported bimetallic cobalt/nickel-organic frameworks (Co–Ni MOFs) that were utilized to enhance faradaic redox reactions, enabling improved energy density. The resulting cobalt/nickel boride/sulfide materials displayed an impressive specific capacitance of 1281 F g^{-1} at a current density of 1 A g^{-1}, excellent rate performance of 802.9 F g^{-1} at 20 A g^{-1}, and outstanding cycling stability with 92.1% capacitance retention after 10 000 cycles.[16] Research in this area has also highlighted the significant potential of emerging pseudocapacitive materials, including 2D nanomaterials such as graphene, transition metal oxides and hydroxides, transition metal dichalcogenides, and metal carbides/nitrides (MXene), for energy storage applications.[17]

All of these findings emphasize the influence of substrate choice and synthesis method on the electrochemical performance of Co_3O_4, highlighting the need for further research to optimize Co_3O_4 deposition on steel substrates with enhanced capacitance and cycling stability for energy storage applications.

Complexing agents are advantageous in controlling the pH of the solution and assist in dispersing particles or controlling the crystal morphology. They significantly influence the properties and stability of the electrode material by affecting the nucleation and growth processes, leading to distinct morphologies and enhanced physicochemical properties. Various complexing agents, like NaOH, HMT, urea, *etc.*, impact the release rate of OH^- ions, resulting in unique morphologies in the synthesized materials. The release rate of OH^- plays a crucial role in shaping the growth environment, which can be finely tuned by adjusting the pH value of the reaction solution.[18] Ammonium chloride (NH_4Cl) influences the nucleation and growth of metal oxides, leading to specific morphologies such as nanoparticles, nanowires, or thin films. NH_4Cl, as a nitrogen source and a pore-forming agent, offers multifaceted benefits in material synthesis[19] and contributes to microstructure evolution with enhanced structural stability.[20] The NH_4OH, as a source of hydroxide ions (OH^-), helps regulate the solution pH and affects the nucleation and growth rates of metal oxide or hydroxide nanoparticles.[21] NH_4F assists in producing more ordered and distinct hierarchical structures,[22] and hexamethylenetetramine (HMT) acts as a chelating agent by forming a stable chelate complex with metal ions, playing a crucial role in stabilizing the structure and improving the overall performance of the supercapacitor. Secondly, as a hydrolyzing agent, HMT undergoes hydrolysis, releasing OH^- ions. These ions play a vital role in the formation of metal hydroxides, which are essential for the electrochemical processes involved in supercapacitors.[23] Wang *et al.* demonstrated that the gradual hydrolysis of urea significantly impacts crystal growth. Through hydrolysis, urea releases OH^- and CO_3^{2-} ions, playing a vital role in promoting good crystallinity, particularly along the longitudinal axis, and favoring the slow and anisotropic growth of nanowires, contributing to their specific characteristics and structural qualities.[24] The incorporation of additives during electrode material synthesis provides a means to regulate morphology and porosity, leading to the production of electrode materials tailored to exhibit advantageous properties for targeted electrochemical applications.

In this study, we aim to improve the electrochemical performance of Co_3O_4 on steel substrates with the assistance of various additives for practical applications in energy storage devices. The electrochemical measurements indicate that Co_3O_4 synthesized in the presence of HMT shows a superior specific capacitance of 468.68 F g^{-1} at a 5 mV s^{-1} scan rate in a 2 M KOH solution. The unique morphology observed with microstructural characterizations of Co_3O_4 grown on a steel substrate using this approach resulted in high capacitance with excellent cycling stability over 10 000 cycles with 98.31% capacitance retention. Furthermore, the development of symmetric supercapacitor devices based on the C-HMT electrodes represents a promising approach for practical applications.

2. Experimental details

Fabrication of Co_3O_4 electrodes

Initially, the substrates (1 cm2) were polished with zero-grade polishing paper and then washed with double-distilled water in an ultrasonic bath for about 20 minutes. All chemicals used were of analytical purity. In the first step, cobalt nitrate hexahydrate ($Co(NO_3)_2{\cdot}6H_2O$, 0.586 g) and urea (CH_4N_2O, 0.120 g) were added to 40 mL of double-distilled water (DDW). The mixture was magnetically stirred for 10 minutes to ensure homogeneity. Subsequently, the solution and a precleaned steel substrate were transferred to a 50 mL Teflon-lined stainless-steel autoclave. The first hydrothermal reaction was carried out at 100 °C for 4 hours. The substrate was then cleaned and subjected to the same hydrothermal reaction process utilizing the same chemicals and concentrations. Finally, the substrate underwent annealing at 300 °C for 4 hours to produce a C-urea thin film sample. Subsequently, samples C-NH_4Cl, C-NH_4OH, C-NH_4F, and C-HMT were prepared using the same steps as for the C-urea sample, with the only variation during the second hydrothermal process, wherein urea was substituted with different chemicals (NH_4Cl (0.107 g), NH_4OH (2 ml), NH_4F (0.070 g), and hexamethylenetetramine (HMT, $C_6H_{12}N_4$, 0.140 g), respectively).

Fabrication of a symmetric supercapacitor device

The symmetric supercapacitor device was developed using the as-prepared C-HMT deposited on a steel substrate as the positive and negative electrode, cellulose paper as the separator, and 2 M KOH as the electrolyte. The device was encapsulated using a flexible plastic film with two copper chips connected to the edges of each electrode for electrical contact. To test its practical application, two of these devices were connected in parallel and used to power five LEDs connected in parallel.

Material characterization and electrochemical measurements

The crystal structures and phase analysis were studied using X-ray powder diffraction (XRD), Raman spectroscopy, and Fourier transform infrared (FTIR) spectroscopy. XRD measurements were conducted using a Bruker D8 Advance X-ray diffractometer using CuKα radiation (~1.54 Å). Raman spectra were obtained using a Renishaw INVIA 0120-20 spectrometer, UK. FTIR spectroscopy was performed using a Bruker spectrometer with a ZnSe Beam Splitter. The SEM (scanning electron microscope) images were captured using a JSM-IT200, JEOL, Japan. The chemical composition and oxidation states were analyzed with X-ray photoelectron spectroscopy (XPS) using an XPS spectrometer (JPS-9030, JEOL Japan). Electrochemical investigations, such as cyclic voltammetry (CV), galvanostatic charge–discharge measurements (GCD), and electrochemical impedance spectroscopy (EIS), were also conducted to evaluate the performance of the Co_3O_4 nanosheets and nanowires in energy storage applications using a BioLogic SP-150e electrochemical workstation. The three-electrode tests were conducted in a 2 M KOH electrolyte, employing a Co_3O_4 thin film as the working electrode, a platinum electrode as the counter electrode, and Ag/AgCl (3 M NaCl) as the reference electrode. The current response changes were studied in CV analysis across various scan rates (100, 80, 60, 40, 20, 10, and 5 mV s^{-1}) within a potential window of 0.0 V to 0.6 V. The GCD tests were performed at 1, 2, 3, 4, and 5 mA cm^{-2} current densities. The EIS was analyzed in a frequency range from 10 mHz to 100 KHz at 0.4 V applied potential concerning the reference electrode.

3. Results and discussion

The synthesis process of the Co_3O_4 nanostructured morphology is schematically depicted in Fig. 1. Initially, during the hydrothermal process, urea ($CO(NH_2)_2$) undergoes hydrolysis in water, leading to the release of hydroxide ions (OH^-), and these hydroxide ions play a crucial role in controlling the formation and morphology of the nanoparticles. Cobalt ions from cobalt nitrate hexahydrate react with hydroxide ions to form the cobalt hydroxide ($Co(OH)_2$) precursor. Ammonia-based compounds

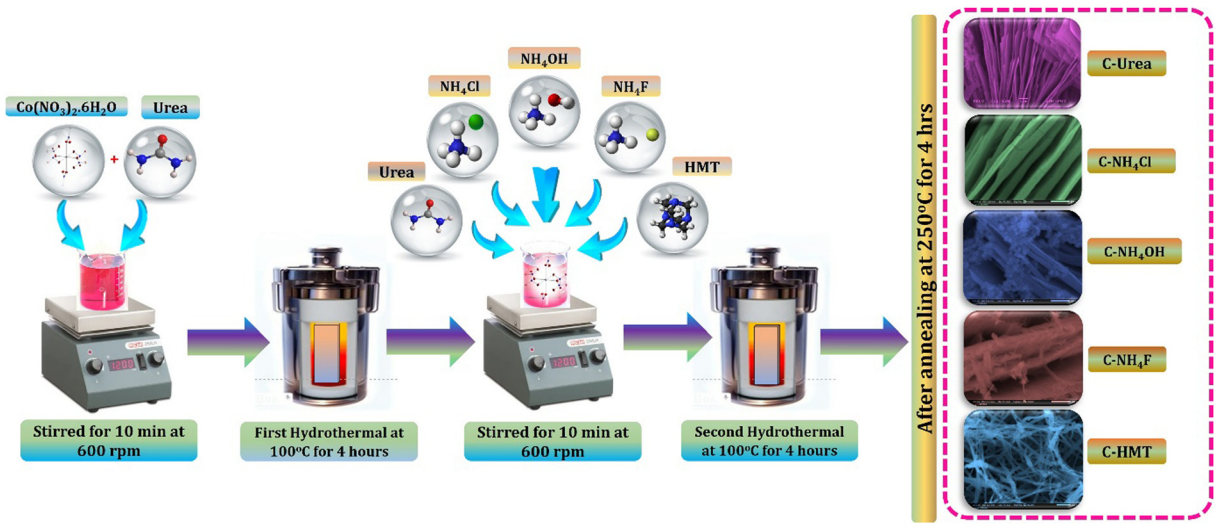

Fig. 1 Schematic illustration showing the synthesis procedure of Co_3O_4.

like NH_4F, NH_4OH, NH_4Cl, and HMT dissociate to form complexes with cobalt ions. These complexes potentially stabilize the cobalt hydroxide precursor. NH_4F and HMT contribute to a slight increase in pH due to the release of ammonia, and NH_4OH significantly increases the pH due to the release of hydroxide ions, while NH_4Cl decreases the pH due to the release of hydronium ions. HMT indirectly affects the pH by releasing ammonia upon decomposition. Finally, during annealing, the cobalt hydroxide precursor undergoes thermal decomposition and oxidation to form cobalt oxide (Co_3O_4) nanostructures. Here, urea and ammonia-based compounds, as a complexing agent, help to precisely control the synthesis conditions, resulting in high-quality Co_3O_4 nanostructures. The structural analysis of the deposited Co_3O_4 nanostructures was conducted using the XRD technique, as illustrated in Fig. 2(a). The diffraction peaks observed at 19.31°, 31.17°, 36.88°, 44.78°, 59.31°, and 65.31° in the XRD patterns are attributed to the crystalline facets (111), (220), (311), (222), (400), (511), and (440), respectively of cubic spinel structured Co_3O_4, as indicated in JCPDS 01-078-1970.[25,26] The steel substrate peaks are denoted by (*) in the pattern and the standard spinel-structured XRD pattern of Co_3O_4 is shown at the bottom with vertical lines. The absence of significant peak shifts in the XRD patterns indicates the high purity of the as-prepared thin films. The crystallite size (D), lattice parameter (a), dislocation density (δ), microstrain (ε), and distortion parameters (g) were calculated using the equations provided in the ESI† for all synthesized samples.[27] The structural and microstructural parameters, such as crystallite size, dislocation density, microstrain, and distortion parameters (g), highlight the intricate interplay between the microstructural features and material properties, as depicted in Table 1. Interestingly, the crystallite sizes of the C-urea, C-NH_4Cl, C-NH_4OH, C-NH_4F, and C-HMT samples were ~19.24 nm, 22.16 nm, 23.94 nm, 20.90 nm and 21.03 nm, respectively. Furthermore, the dislocation density and lattice distortion are higher for the C-urea samples, attributed to the density of crystallographic defects and smaller crystallite sizes, resulting in a higher density of grain boundaries and dislocations.[28]

The molecular structure, chemical bonding configuration, and functional groups are qualitatively studied by FT-IR analyses, as shown in Fig. 2(b). In the FTIR spectrum, two sharp peaks were detected around 672 cm^{-1} and 573 cm^{-1}, corresponding to the Co^{2+}–O and Co^{3+}–O stretching vibration modes, respectively, resulting from the tetrahedral (Co^{3+}) and octahedral sites (Co^{2+}) of the spinel structure of the Co_3O_4.[29] The bands at 3421 cm^{-1} and 1638 cm^{-1} are due to the O–H stretching vibration

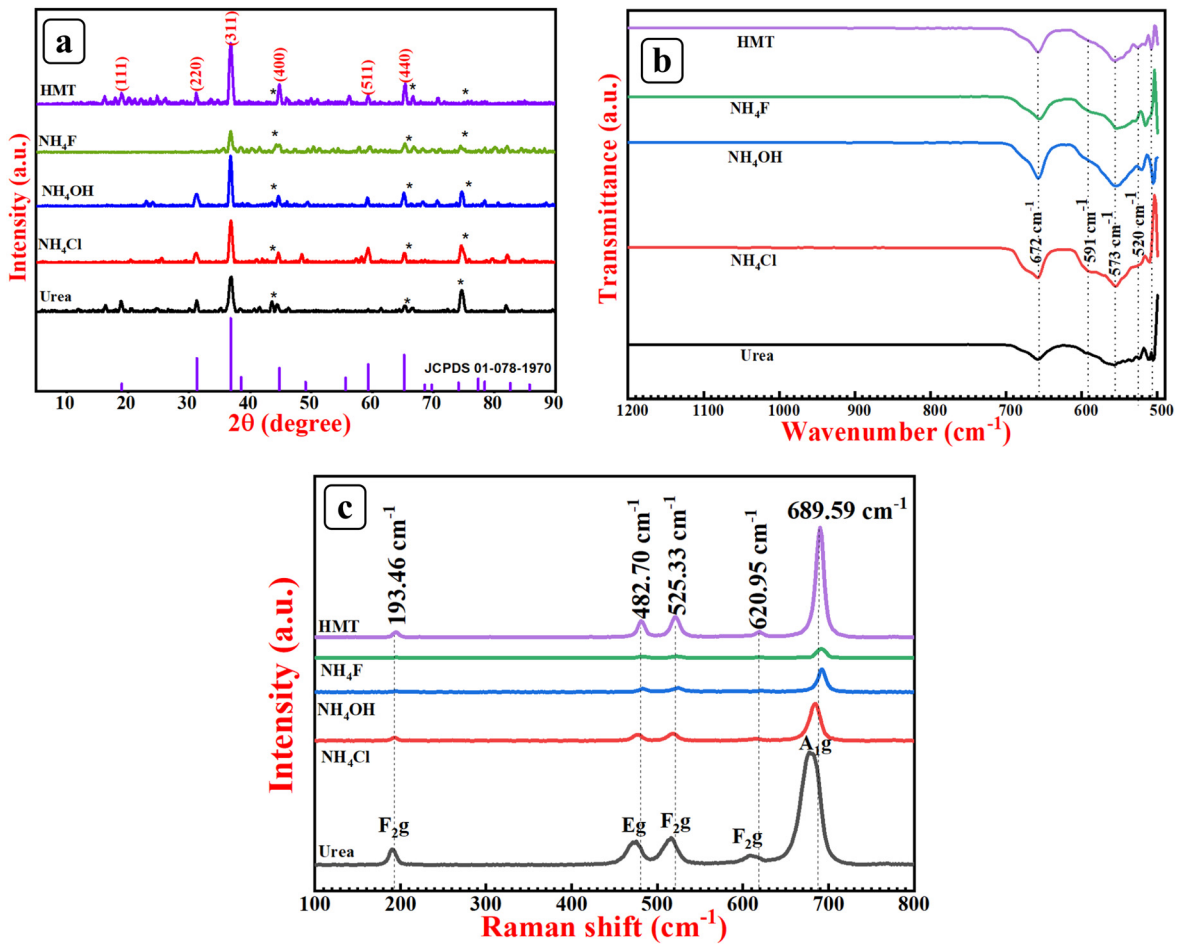

Fig. 2 (a) XRD pattern, (b) FTIR spectrum and (c) Raman spectrum of the synthesized C-urea, C-NH_4Cl, C-NH_4OH, C-NH_4F, and C-HMT thin films.

Table 1 Structural and microstructural parameters of Co_3O_4 nanosheets and nanowires prepared by a hydrothermal method with various additives

Samples	Crystallite size D (nm)	Dislocations density (δ) $\times 10^{20}$ (lines per m^2)	Microstrain (ε)	Distortion parameters (g)
C-urea	19.24	0.27	0.064	0.023
C-NH_4Cl	22.16	0.20	0.061	0.023
C-NH_4OH	23.94	0.17	0.061	0.021
C-NH_4F	20.90	0.23	0.059	0.022
C-HMT	21.03	0.23	0.059	0.026

mode for the adsorbed water molecules and the bending mode of water molecule vibration, respectively.[30,31] As shown in Fig. 2(c), the Raman spectrum of the Co_3O_4 nanosheets and nanowires shows five active peaks located at around 193 cm^{-1}, 484 cm^{-1}, 524 cm^{-1}, 623 cm^{-1}, and 692 cm^{-1} corresponding to the F_{2g}, E_g, F^1_{2g}, F^2_{2g}, and A^1_{1g} modes of Co_3O_4, respectively, and which are consistent with the pure crystalline Co_3O_4. The peak positions of the five active modes shift slightly in the synthesized Co_3O_4 nanosheets and nanowires. This can be attributed to the optical phonon confinement effect, where the dimensions of the nanostructures influence the vibrational modes of the optical phonons in a material.[32]

SEM analysis was conducted to examine the nanostructured morphology of the hydrothermally deposited C-urea, C-NH_4Cl, C-NH_4OH, C-NH_4F, and C-HMT thin films, as shown in Fig. 3(a)–(e) at various magnifications. The morphological analysis revealed the stacking of the nanosheets, resembling the arrangement of a deck of cards for C-urea, C-NH_4Cl, C-NH_4OH, and C-NH_4F. Within this arrangement, each layer, much like a card in a deck, exhibited well-defined and straight separation from its adjacent layers, emphasizing the ordered and distinct nature of the nanosheets arrangement. However, the C-HMT thin films exhibited nanowire morphological features. The SEM images of NH_4Cl revealed well-separated nanosheets, with sizes ranging from 115–215 nm (Fig. 3(b_1)–(b_4)). In contrast, the nanosheets obtained after NH_4OH and NH_4F treatment displayed an uneven distribution of nanospheres on the nanosheets, approximately 60 nm and 40 nm in diameter, respectively, covering the surface (Fig. 3(c_1)–(c_4) and (d_1)–(d_4)). Compared to all other samples, nanowires obtained with HMT treatment were thinner, having diameters in the range of 10 to 34 nm (Fig. 3(e_1)–(e_4)). This observation highlights the unique influence of the HMT treatment on the diameter of the nanowires, distinguishing it from the size characteristics of the nanosheets produced under different treatments. This distinct morphological observation highlights the impact of various additives on the resulting nanostructures, emphasizing variations in the size, growth, and distribution patterns of the synthesized Co_3O_4 thin films. The C-HMT sample exhibited a uniform distribution of nanowires (Fig. 3(e_4)), which is advantageous for facilitating the effective percolation of the electrolytes, thus enabling easier ion migration and maximizing the utilization of active areas for charge transfer reactions.

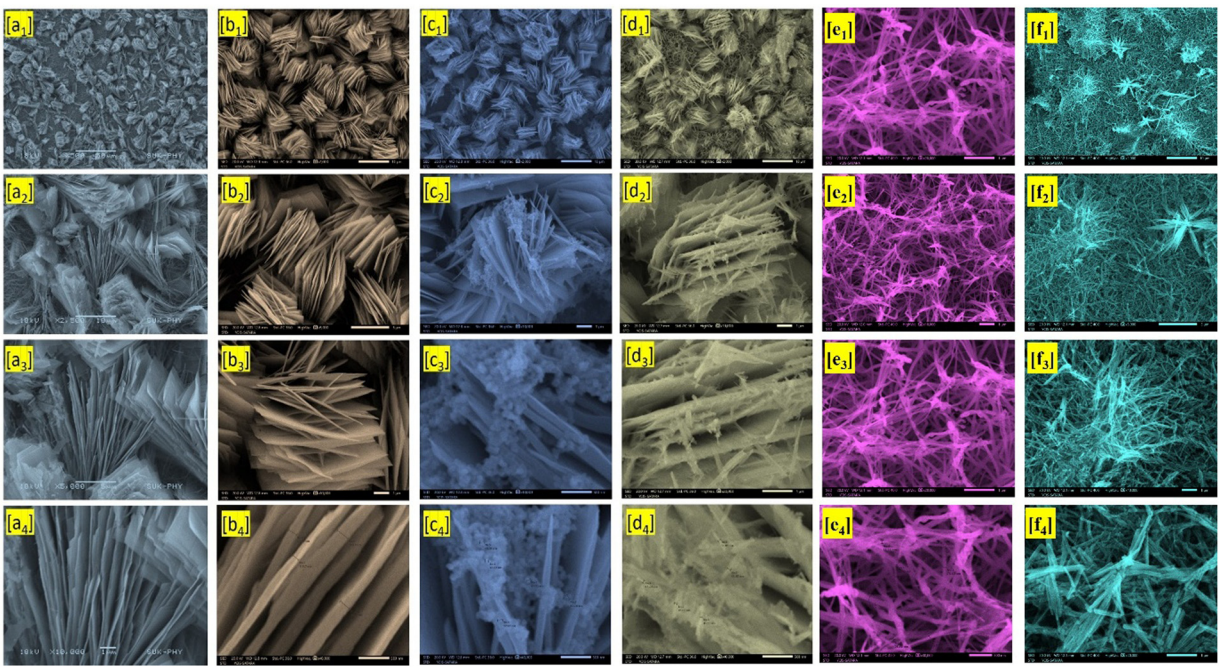

Fig. 3 SEM images of Co_3O_4 samples: (a_1)–(a_4) C-urea, (b_1)–(b_4) C-NH_4Cl, (c_1)–(c_4) C-NH_4OH, (d_1)–(d_4) C-NH_4F, (e_1)–(e_4) C-HMT, and (f_1)–(f_4) post-cycling SEM analysis of C-HMT after 10 000 cycles at various magnifications.

The transmission electron microscopy (TEM) analysis reveals that the Co_3O_4 nanowires exhibit a well-defined one-dimensional morphology with uniform and elongated structures. Fig. 4(a) and (b) depict nanowires with diameters ranging from 10 to 34 nm and lengths extending to several nanometers, which is consistent with the XRD and SEM results. The high-resolution TEM images (Fig. 4(c)) provide insights into the atomic arrangement within the nanowires, enabling the measurement of interplanar spacings. These spacings of ~0.276 nm, 0.239 nm, and 0.203 nm correspond to the {(220), (311), and (400)} crystal planes, further confirming the crystalline phase and structural integrity of Co_3O_4. Additionally, the selected area electron diffraction (SAED) pattern (Fig. 4(d)) obtained through TEM confirms the crystalline structure of these nanowires. The SAED pattern displays concentric diffraction rings at interplanar spacings of 0.467 nm, 0.284 nm, 0.244 nm, 0.200 nm, 0.156 nm, and 0.143 nm, which correspond to the lattice planes {(111), (220), (311), (400), (511), (440)} of the spinel Co_3O_4 phase, consistent with the cubic spinel structure as per the JCPDS file 01-078-1970.[20]

The porosity and specific surface area (SSA) of the Co_3O_4 thin films were assessed using BET N_2 gas-sorption measurements, as presented in Fig. 4(e) and (f). The nitrogen adsorption–desorption isotherms (Fig. 4(e)) exhibit a hysteresis loop characteristic of mesoporous materials, indicating a type IV isotherm that results from capillary condensation within the mesopores. The BET analysis revealed a specific surface area of approximately 47.5 $m^2\ g^{-1}$ and a pore volume of 0.2301 $cm^3\ g^{-1}$. Additionally, the BJH pore size distribution curve (Fig. 4(f)) suggests a uniform pore structure with an average pore diameter of 5.35 nm. This mesoporous architecture incorporates both micropores (<2 nm) and mesopores (2–50 nm), offering a high surface-to-volume ratio and abundant active sites. Such structural features are particularly beneficial for energy storage applications, where a well-optimized pore structure enhances the electrochemical performance.

The observed mesoporosity and pore size distribution align with previous studies on similar materials. For example, Gaikar *et al.* documented type IV isotherms in electrodeposited synthesized Co_3O_4 and attributed the enhanced electrochemical behavior to its mesoporous structure.[33] Similarly, Hou *et al.* highlighted that Co_3O_4 with well-defined microspherical mesoporous networks demonstrated superior energy storage performance. These findings emphasize the importance of mesoporous structures in optimizing the functional properties of Co_3O_4-based thin films and nanostructures, making them highly suitable for advanced energy storage technologies.[34]

X-ray photoelectron spectroscopy (XPS) analysis provides valuable information about the elemental composition and oxidation state of the cobalt and oxygen in the developed thin

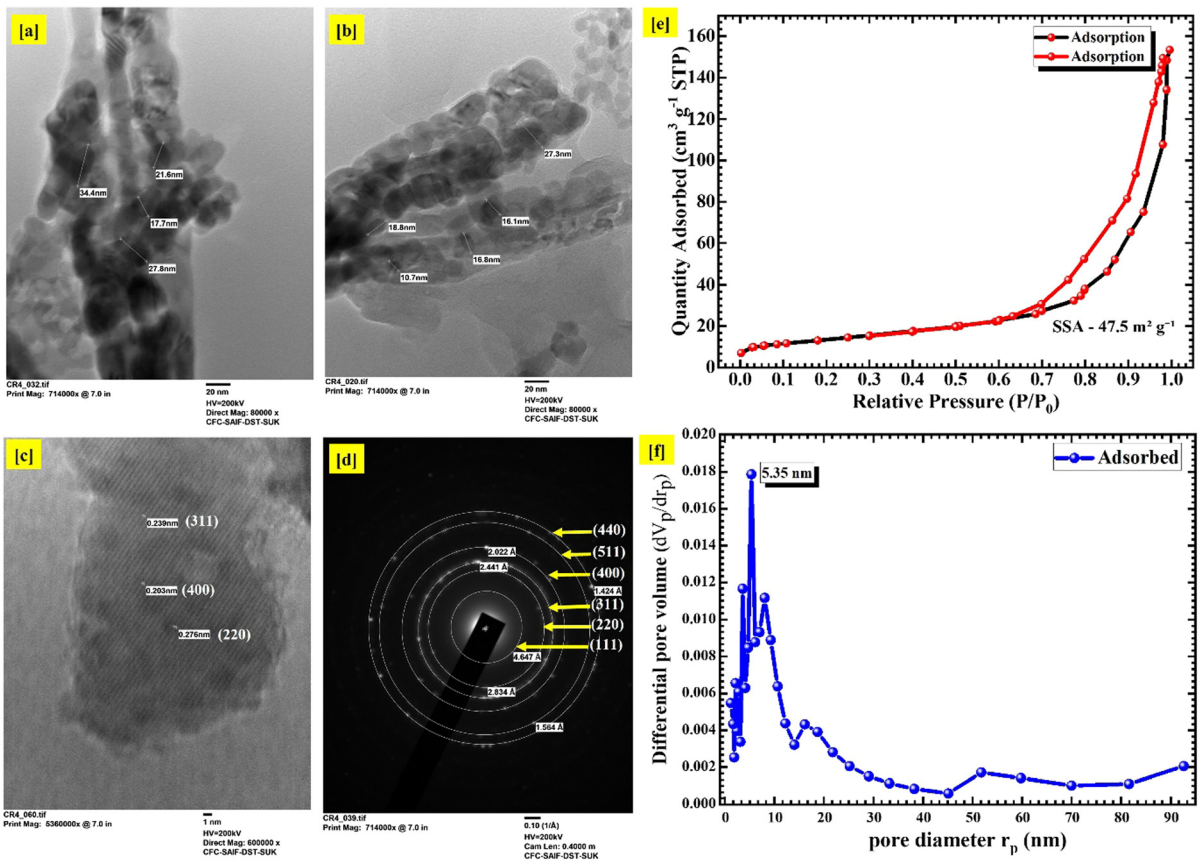

Fig. 4 (a) and (b) TEM images of Co_3O_4 nanowires, (c) high-resolution TEM image and (d) selected area electron diffraction (SAED) pattern, (e) the N_2 adsorption/desorption isotherm surface area analysis and (f) the pore size distribution of the Co_3O_4 thin film electrode.

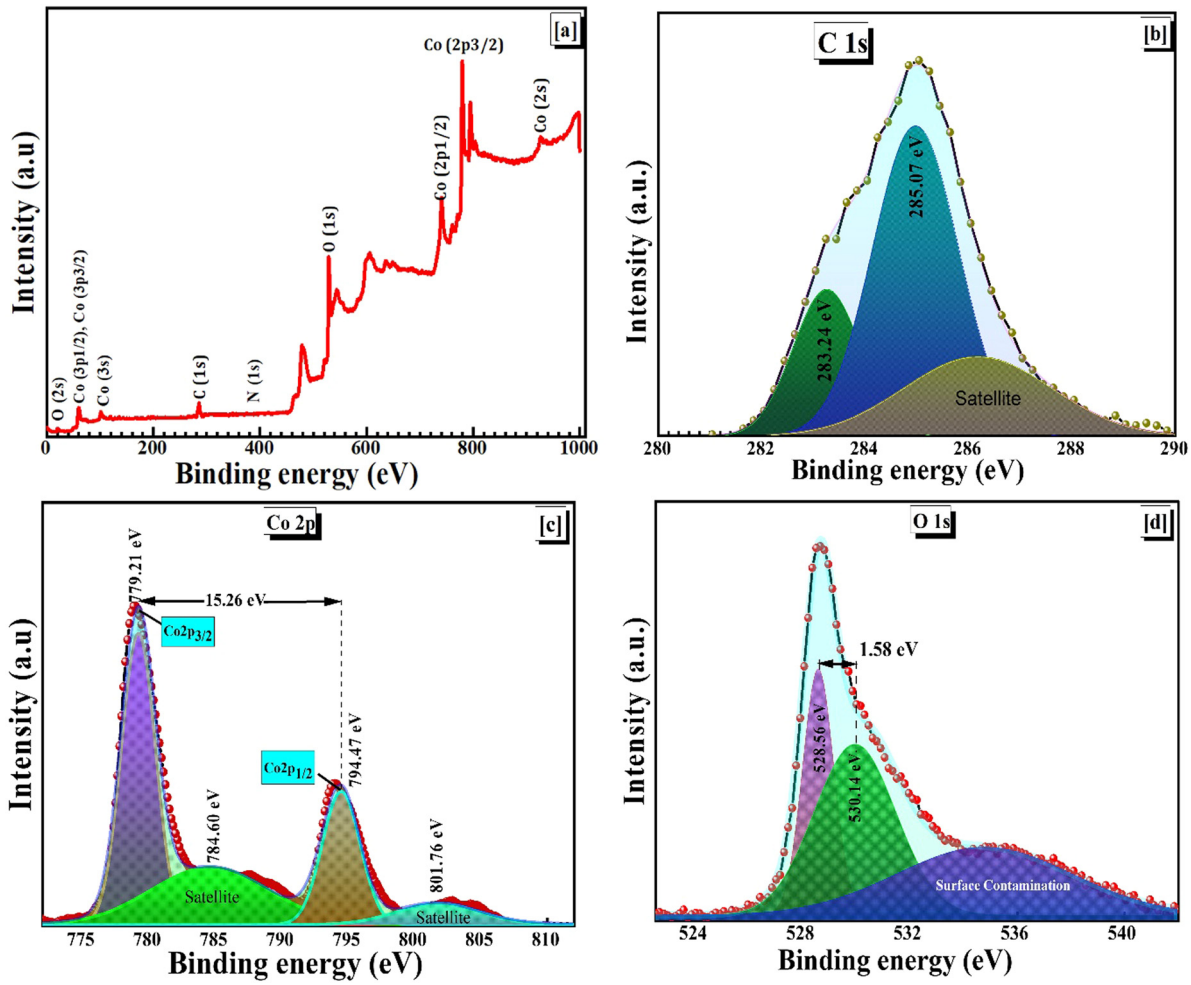

Fig. 5 XPS spectra of C-HMT thin films: (a) survey spectrum and high resolution (b) C 1s, (c) Co 2p and (d) O 1s spectra.

films. The high-resolution XPS survey spectrum, as depicted in Fig. 5(a), exhibits peaks corresponding to carbon (C 1s), oxygen (O 1s), and cobalt (Co 2p) core levels. Fig. 5(b) illustrates that the peaks at 285.07 eV correspond to C–C bonds, and the peak around 287.7 eV is attributed to C–O bonds, indicating the presence of oxygen-containing functional groups.[35] Fig. 5(c) illustrates the core level spectra of Co 2p, providing information about the oxidation states of cobalt in the Co_3O_4 sample, which are observed at around 779.21 eV (Co $2p_{3/2}$) and 794.47 eV (Co $2p_{1/2}$), corresponding to the Co^{2+} and Co^{3+} oxidation states, respectively. The energy separation between the Co $2p_{3/2}$ and Co $2p_{1/2}$ peaks is around 15.26 eV, indicating spin–orbit splitting. Furthermore, multiple splitting and shake-up processes result in satellite peaks in the XPS spectrum. The peaks around 784.60 eV and 801.76 eV are attributed to the interaction between valence and core-level electrons. Moreover, Fig. 5(d) presents the high-resolution oxygen (O 1s) spectrum, revealing two peaks around 530.14 eV and 528.56 eV, associated with absorbed oxygen species and lattice oxygen (O^{2-}) in the synthesized C-HMT electrode.[36]

The cathodic and anodic charge density behavior of hydrothermally deposited C-urea, C-NH_4Cl, C-NH_4OH, C-NH_4F, and C-HMT thin films was examined by cyclic voltammetry (CV). As depicted in Fig. S1 (ESI†), the CV curves were analyzed using a three-electrode electrochemical setup with a potential window ranging from 0 to 0.6 V *versus* Ag/AgCl in a 2 M KOH electrolyte.

A comprehensive analysis of the charge storage and release dynamics was conducted by studying the CV profiles at various scan rates, ranging from 5 mV s^{-1} to 100 mV s^{-1}. Fig. 6(a) illustrates the CV profile of the C-HMT sample at different scan rates. The CV curves are characterized by the two distinct pairs of redox peaks during the anodic and cathodic sweeps, attributed to the quasi-reversible redox reaction occurring on the Co_3O_4 surface. In a quasi-reversible redox reaction, the anodic peak corresponds to the oxidation process, where Co^{2+} ions are oxidized to a higher oxidation state, Co^{3+}. Conversely, during the cathodic peak, the reduction process occurs, leading to the reduction of Co^{3+} ions back to the lower oxidation state of Co^{2+}, indicating that the samples exhibit pseudocapacitive properties. The reversible redox reactions taking place are as follows[37]

$$Co_3O_4 + OH^- + H_2O \leftrightarrow 3CoOOH + e^- \quad (1)$$

$$CoOOH + OH^- \leftrightarrow CoO_2 + H_2O + e^- \quad (2)$$

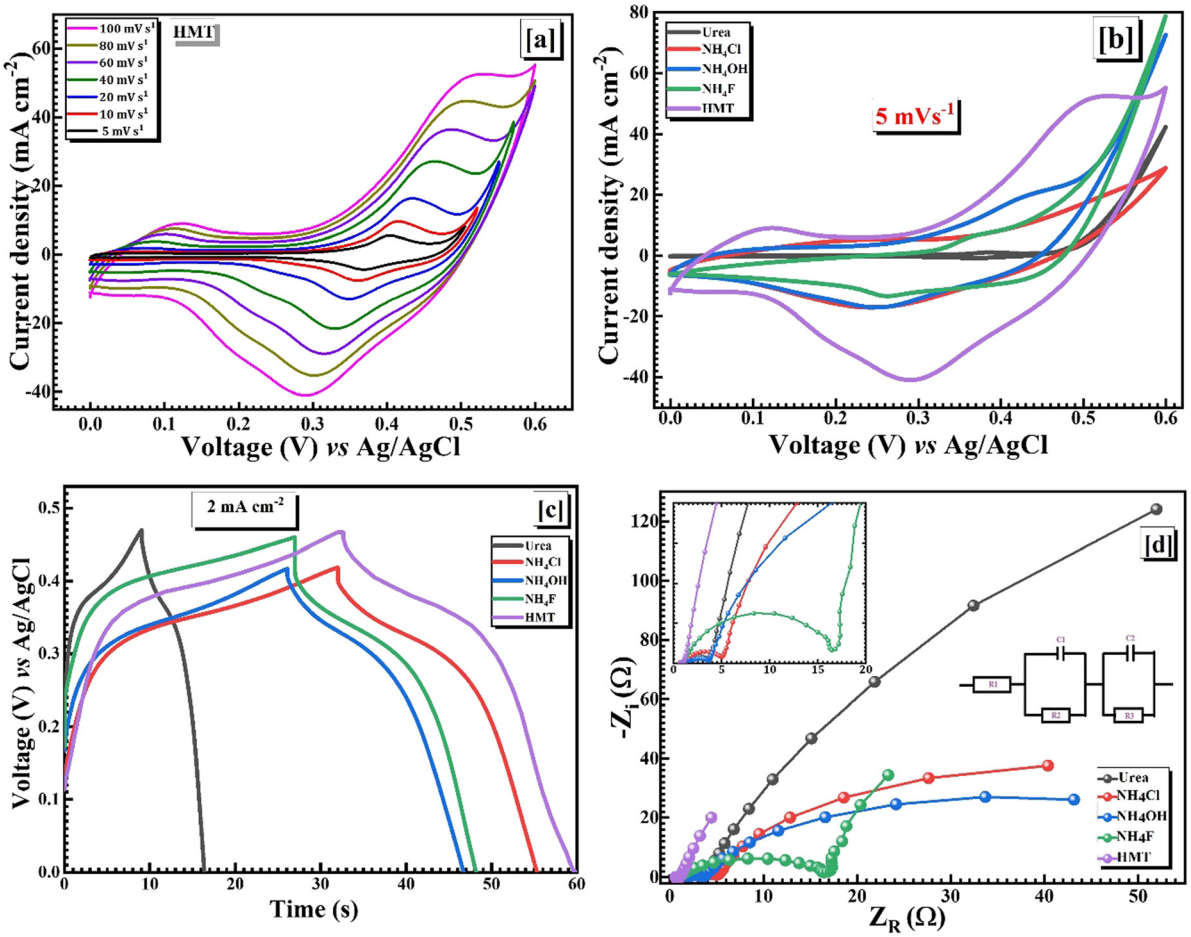

Fig. 6 (a) CV profile of the C-HMT electrodes at various scan rates (5, 10, 20, 40, 60, 80, and 100 mV s^{-1}), (b) CV, (c) GCD and (d) Nyquist plots (the inset shows the enlargement image and equivalent circuit of the C-HMT electrode) of all synthesized electrodes.

As the scan rate increases from 5 to 100 mV s^{-1}, the enclosed area is observed to increase gradually. In addition, the pair of redox peaks shifts to higher and lower potentials, respectively.[38] The shifting of the peaks may result from the polarization effect, which includes concentration and electrochemical polarization.[39] At high scan rates, the rate of electron transfer between the electrode and the electrolyte increases, leading to higher current peaks observed in the CV curves.

Fig. 6(b) illustrates the comparative study of the CV profile of all-synthesized samples conducted at 5 mV s^{-1}. The area enclosed by the C-HMT sample exceeds that of all other samples, indicating a higher charge storage capacity and increased electrochemical activity. Specifically, the specific capacitance recorded at a scan rate of 5 mV s^{-1} was 468.68 F g^{-1}, 212.28 F g^{-1}, 178.05 F g^{-1}, 155.18 F g^{-1}, and 103.72 F g^{-1} for the C-HMT, C-NH_4Cl, C-NH_4OH, C-NH_4F, and C-urea thin films, respectively. The superior performance of the Co_3O_4 electrodes in the presence of HMT is attributed to their nanowire morphology, which provides more active sites for electrochemical reactions and enhances ion diffusion, electrolyte penetration, and ion transport within the electrode. Specifically, the uniform thin nanowires in the C-HMT sample facilitate easier ion migration to the electrode–electrolyte interface and ensure active utilization of the available electrode area. The observed specific capacitance in the present study is higher than that of the reported values, and a detailed comparative study has been given in Table S2 (ESI†).

Fig. S2 (ESI†) shows the GCD curves of the synthesized samples with a potential window of 0–0.5 V at current densities ranging from 1 to 5 mA cm^{-2}. It shows a significant difference in cycling time with a change in current density from 1 mA cm^{-2} to 5 mA cm^{-2}, attributed to limitations in the reaction rates, diffusion processes, and electrochemical stability. These factors collectively cause less efficient energy storage and faster charge depletion at higher current densities. The GCD analysis of all samples was performed at a current density of 2 mA cm^{-2}, as shown in Fig. 6(c). The GCD profiles exhibit a blend of capacitive and battery-type behavior in the synthesized samples, characterized by an initial voltage drop attributed to capacitive behavior followed by a phase transformation plateau, allowing reactants to diffuse into the inner pores for battery-type reactions. All electrodes display symmetrical GCD profiles with distinct potential plateaus. The charge storage mechanism was investigated by studying the anodic and cathodic peak current density *vs.* scan

rate relationship, as shown in Fig. S3 (ESI†), which shows the linear relationship. The inset of Fig. S3 (ESI†) shows the linear relationship between the peak current density and the square root of the scan rate for the respective samples. The data was analyzed according to the relation given by,

$$i = av^b \quad (3)$$

or

$$\log i = b \log v + \log a \quad (4)$$

a and b are constants. More importantly, the slope of the plot of the logarithm of the anodic and cathodic peak current density *versus* the logarithm of scan rate for the C-HMT nanowires was found to be 0.99 and 0.993 for the anodic and cathodic curves (Fig. 7(b)). The value of "b" calculated from the log(i) *vs.* log(v) graph for C-HMT nanowires, ranging between 0.5 to 1 for both cathodic and anodic peaks, suggests a behavior closely resembling a semi-infinite diffusion-controlled process. When "b" approaches 1, it indicates that the electrode process is predominantly surface-controlled, implying significant contributions from both capacitive and pseudocapacitive mechanisms.[40] This suggests that the capacity of C-HMT originates from a synergistic combination of capacitive control and pseudocapacitive surface-controlled electrode processes.

Electrochemical impedance spectroscopy (EIS) provides valuable information about the impedance of supercapacitors. This technique involves applying a small voltage amplitude at a specific potential over a wide range of frequencies, typically from 10 mHz to 100 kHz. The resulting EIS data is represented graphically as a Nyquist plot, as shown in Fig. 6(d) (Fig. S4, ESI†) of the developed thin films. Typically, the Nyquist plot exhibits three distinct regions: a semicircle at high frequency ($>10^4$ Hz) representing the interface resistance between the electrode and electrolyte, an intermediate frequency region (10^4 to 1 Hz) that connects the semicircle to the low-frequency region indicating pseudo-charge or charge transfer resistance, and a nearly vertical line along the imaginary axis at low frequency (less than 1 Hz), signifying capacitive behavior. The inset in Fig. 6(d) shows the equivalent circuit employed for fitting. R_1 represents the resistances caused by the migration of ions through the electrolyte (solution resistance), R_2 is the contact resistance or the resistance caused by the electrode–electrolyte interface film (SEI layer), and R_3 is the charge transfer on the electrode. Constant phase elements C_1 and C_1 are used to analyze imperfect dielectric layer capacitors affected by electrode inhomogeneities, mainly due to variations in the

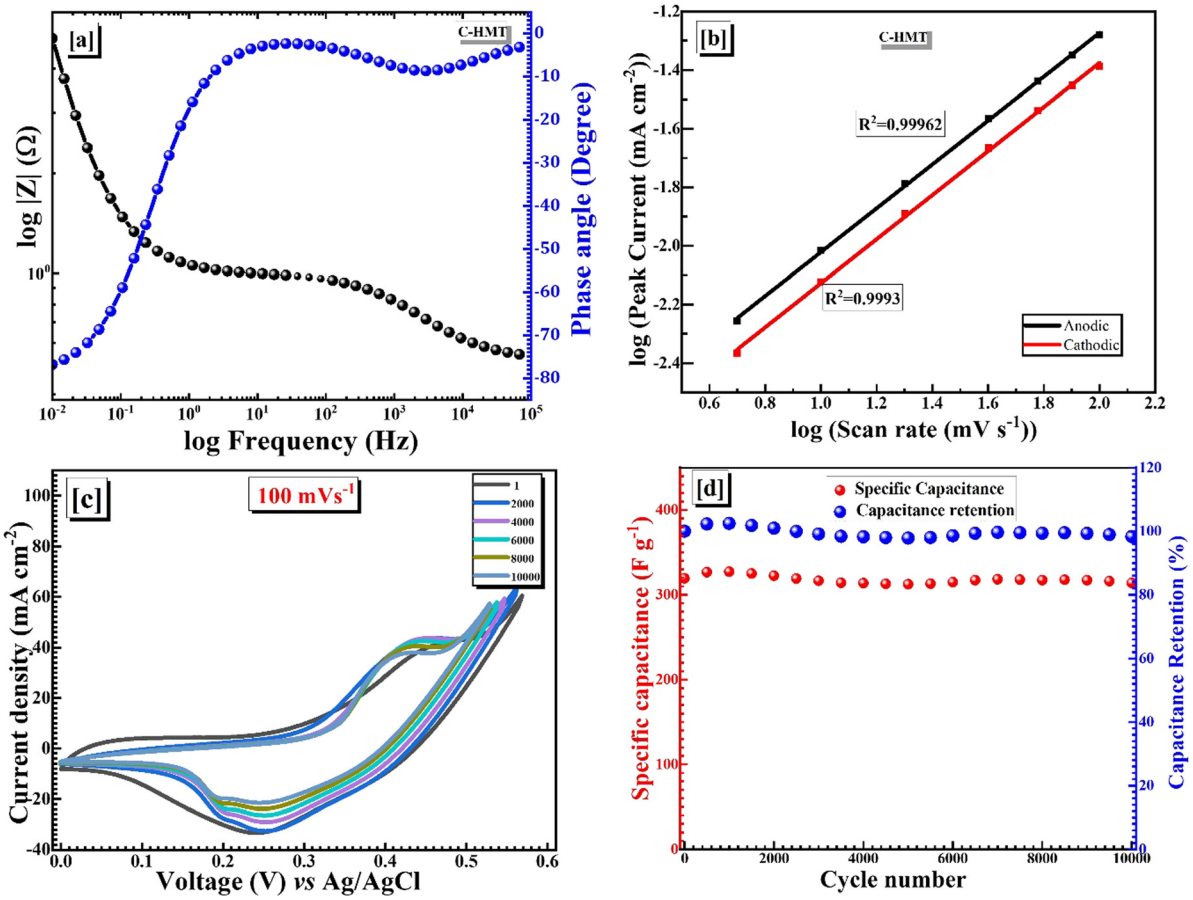

Fig. 7 (a) Bode plot, (b) variation of log of peak current *vs.* log of scan rate, (c) cycling stability and (d) variation in specific capacitance and coulombic efficiency as a function of the cycle number of the C-HMT electrode.

dimensions and nanostructures of the active materials.[41] The charge transfer resistance is higher for the C-NH_4F thin films than for all other samples, while it is lower for the C-HMT nanowires.

Fig. 7(a) represents the Bode plot of the C-HMT; in the lower frequency region, the maximum phase angle was between 60° and 75°, thus confirming the pseudocapacitive nature of the synthesized electrode. In electrochemical systems, a phase angle near 90 degrees indicates ideal capacitive behavior, while lower angles signify contributions from faradaic processes. The observed phase angle suggests that the charge storage mechanism involves both capacitive effects and fast, reversible redox reactions at the electrode surface. This combination is a characteristic feature of pseudocapacitive materials, where the faradaic reactions contribute significantly to enhancing charge storage. Such behavior makes the synthesized electrode highly suitable for energy storage applications, offering a balance of high energy density and efficient charge–discharge capabilities. The stability performance of the C-HMT electrode was evaluated at a scan rate of 100 mV s^{-1} for 10 000 cycles, as depicted in Fig. 7(c). Cycling stability is a critical parameter for evaluating the performance of energy storage devices. As depicted in Fig. 6(d), an initial increase in capacitance was observed, achieving 100% retention at 2000 cycles, with a specific capacitance of 322.36 F g^{-1} at a scan rate of 100 mV s^{-1}. This behavior is attributed to the electrochemical activation of the electrode material, which enhances wettability and facilitates ion diffusion during the early cycles. Repeated cycling further improves the accessibility of active sites, thereby enhancing charge storage efficiency. Following the initial activation phase, only a minimal decrease in capacitance was noted, with the electrode maintaining a capacitance of 313.95 F g^{-1} at the 10 000th cycle. Throughout the cycling process, the capacitance remained consistently stable. Furthermore, post-cycling scanning electron microscopy (SEM) analysis (Fig. 3(f_1)–(f_4)) was conducted on the electrode after completing 10 000 cycles to evaluate its structural integrity. The SEM images reveal that the nanowire morphology is largely preserved, with only minimal breakage observed. This suggests that the electrode exhibits excellent structural stability during prolonged cycling. The exceptional capacity retention of 98.13% after 10 000 cycles underscores the ability of C-HMT to effectively maintain its electrochemical properties over repeated charge–discharge cycles, demonstrating outstanding cycling stability with minimal degradation or loss of active material during cycling. A C-HMT//C-HMT symmetric device was assembled to examine the performance of the C-HMT electrode. Fig. 8(a) shows the CV profile at various scan rates of 5, 10, 20, 40, 60, 80, and 100 mV s^{-1} of the designed symmetric supercapacitor device. The CV profiles reveal a rapid surface redox reaction, characteristic of pseudocapacitive behavior,

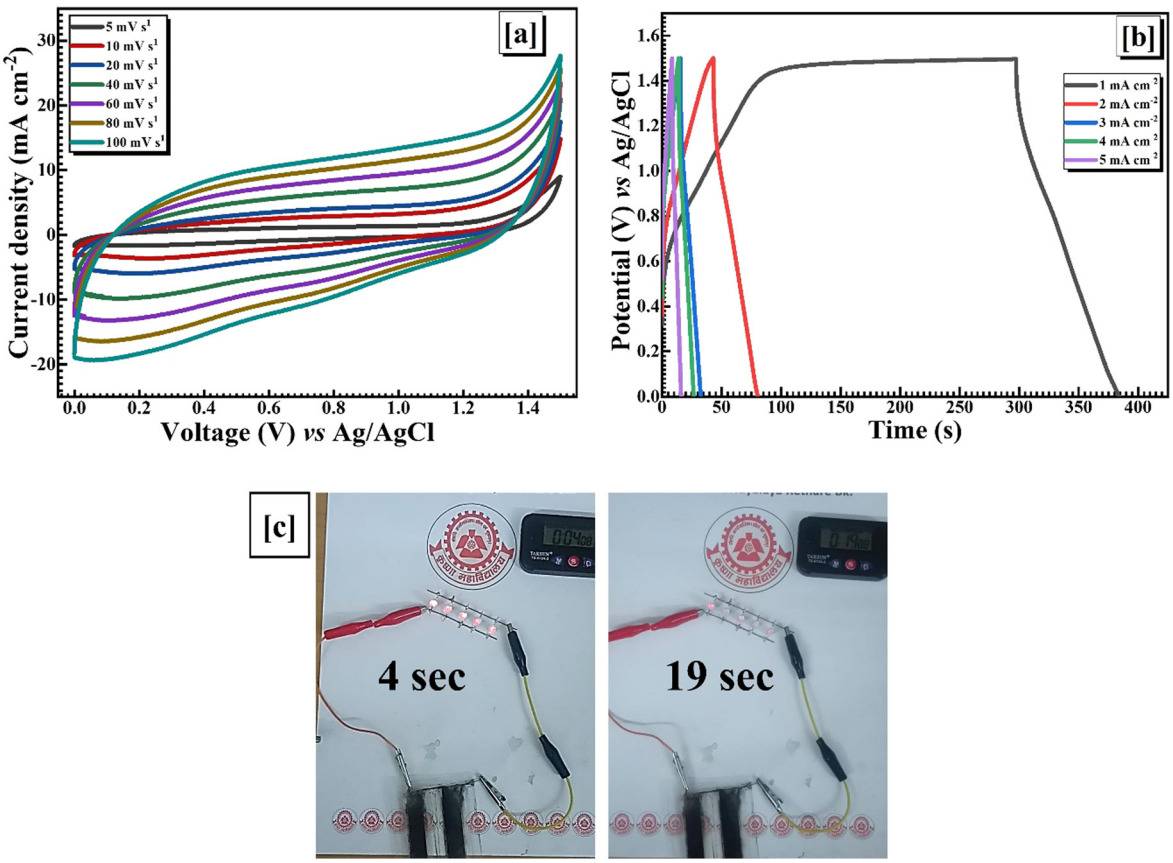

Fig. 8 (a) CV profile at various scan rates (5, 10, 20, 40, 60, 80, and 100 mV s^{-1}), (b) GCD analysis at various current densities, (c) digital photographs of the synthesized symmetric supercapacitor device based on the C-HMT electrode lighting up 5 LEDs connected in parallel after 4 and 19 seconds.

indicative of a capacitor-type electrode signature.[42] Fig. 8(b) depicts the GCD profile of the device acquired at various current densities. It shows a shorter discharge time relative to the charging time, suggesting that not all the charge stored during charging is effectively recovered during discharge. This discrepancy indicates losses within the system, such as incomplete charge utilization or side reactions occurring during the charge and discharge processes. Fig. 8(c) displays digital photographs of the working model of the synthesized device, which was analyzed by connecting two such devices in parallel. This parallel combination of two symmetric devices, after charging for 10 s, was able to light up five red LEDs connected in parallel for 20 seconds.[43–45]

4. Conclusions

This study showcased the development of Co_3O_4 nanostructures on a steel substrate using the double hydrothermal approach. The incorporation of additives has revolutionized the synthesis strategy, resulting in a film prepared in the presence of HMT that exhibits a superior specific capacitance of 468.68 F g^{-1} at a scan rate of 5 mV s^{-1}. Remarkably, the electrode retained 98.31% of its initial capacitance even after 10 000 cycles at a scan rate of 100 mV s^{-1}. This superior electrochemical performance can be attributed to the unique nanowires of the active material that grew uniformly, facilitated by the use of a complexing agent. This study also demonstrated the practical use of the synthesized symmetrical supercapacitor device, as two synthesized devices based on C-HMT electrodes powered five LEDs for 20 seconds when connected in parallel. These results show the advantageous role of additives in controlling morphology and enhancing stability, ultimately leading to improved performance in supercapacitor applications. The findings of this study could potentially shape the future of supercapacitor technology and inspire further research and innovation in this field.

Author contributions

RSD: writing the original draft, methodology, and investigation; VSJ: assisted in experiments and calculations, methodology, software, assisted in characterizations; SRP: assisted in experiments and calculations; PSP: supervision, review & editing, formal analysis; RHM: characterizations, assisted in review and editing original draft, funding acquisition; AKY: characterizations, review and editing, formal analysis; DSD: supervision, writing – review & editing, project administration, funding acquisition.

Data availability

The data supporting this study's findings are available from the corresponding author upon request.

Conflicts of interest

The authors declare no conflict of interest.

Acknowledgements

One of the authors, Mr. Vinayak S. Jadhav and Dr D. S. Dalavi, is thankful to the Department of Science and Technology, Science and Engineering Research Board (DST-SERB), New Delhi, India for financial support through the Empowerment and Equity Opportunities for Excellence in Science (EMEQ) scheme (EEQ/2021/000984). The author Mrs Radhika. S. Desai would like to acknowledge the Chhatrapati Shahu Maharaj Research Training and Human Development Institute (SARTHI), Pune (Government of Maharashtra) for the financial support under the Chhatrapati Shahu Maharaj National Research Fellowship-2021. The authors are also grateful to the Researchers Supporting Project number (RSP2025R222), King Saud University, Riyadh, Saudi Arabia, for the financial support.

Notes and references

1 W. L. Jia, J. Li, Z. J. Lu, Y. F. Juan and Y. Q. Jiang, *J. Alloys Compd.*, 2020, **815**, 152373.
2 H. Xia, D. Zhu, Z. Luo, Y. Yu, X. Shi, G. Yuan and J. Xie, *Sci. Rep.*, 2013, **3**, 1–8.
3 J. B. Wu, Y. Lin, X. H. Xia, J. Y. Xu and Q. Y. Shi, *Electrochim. Acta*, 2011, **56**, 7163–7170.
4 D. You, J. Lou, X. Li, Y. Zhou, X. Sun and X. Wang, *J. Power Sources*, 2021, **494**, 229775.
5 X. Pan, X. Chen, Y. Li and Z. Yu, *Electrochim. Acta*, 2015, **182**, 1101–1106.
6 C. W. Kung, H. W. Chen, C. Y. Lin, R. Vittal and K. C. Ho, *J. Power Sources*, 2012, **214**, 91–99.
7 R. Tummala, R. K. Guduru and P. S. Mohanty, *J. Power Sources*, 2012, **209**, 44–51.
8 A. D. Jagadale, V. S. Kumbhar and C. D. Lokhande, *J. Colloid Interface Sci.*, 2013, **406**, 225–230.
9 S. V. Khavale and B. J. Lokhande, *J. Mater. Sci.: Mater. Electron.*, 2017, **28**, 5106–5115.
10 P. S. Gaikar, S. T. Navale, V. V. Jadhav, P. V. Shinde, D. P. Dubal, P. R. Arjunwadkar, F. J. Stadler, M. Naushad, A. A. Ghfar and R. S. Mane, *Electrochim. Acta*, 2017, **253**, 151–162.
11 S. S. Gavande, Y. H. Navale, A. S. Salunkhe, S. Gavande, P. S. Kulkarni and B. R. Karche, *J. Nano- Electron. Phys.*, 2020, **12**, 1–8.
12 S. S. Gavande, A. S. Salunkhe, Y. H. Navale, S. Gavande, P. S. Kulkarni and B. R. Karche, *AIP Conf. Proc.*, 2020, **2265**, 5–9.
13 G. Wang, X. Shen, J. Horvat, B. Wang, H. Liu, D. Wexler and J. Yao, *J. Phys. Chem. C*, 2009, **113**, 4357–4361.
14 L. Cui, J. Li and X. G. Zhang, *J. Appl. Electrochem.*, 2009, **39**, 1871–1876.
15 P. Nakhanivej, X. Yu, S. K. Park, S. Kim, J.-Y. Hong, H. J. Kim, W. Lee, J. Y. Hwang, J. E. Yang, C. Wolverton,

J. Kong, M. Chhowalla and H. S. Park, *Nat. Mater.*, 2019, **18**, 156–162.
16 Q. Wang, Y. Luo, R. Hou, S. Zaman, K. Qi, H. Liu, H. S. Park and B. Y. Xia, *Adv. Mater.*, 2019, **31**(51), 905744.
17 X. Yu, S. Yun, J. S. Yeon, P. Bhattacharya, L. Wang, S. W. Lee, X. Hu and H. S. Park, *Adv. Energy Mater.*, 2018, **8**(13), 1702930.
18 R. S. Desai, V. S. Jadhav, P. S. Patil and D. S. Dalavi, *Mater. Adv.*, 2024, **5**, 920–960.
19 G. Li, F. Liu, W. Ma, H. Li and S. Li, *Molecules*, 2023, **28**, 5648.
20 W. Guo, T. Yang, L. Huang and S. Wang, *J. Energy Storage*, 2021, **44**, 103472.
21 H. R. Abid, H. M. Ang and S. Wang, *Nanoscale*, 2012, **4**, 3089–3094.
22 Z. Yu, Z. Cheng, Z. Tai, X. Wang, C. M. Subramaniyam, C. Fang, S. Al-Rubaye, X. Wang and S. Dou, *RSC Adv.*, 2016, **6**, 45783–45790.
23 A. Umar, S. D. Raut, A. A. Ibrahim, H. Algadi, H. Albargi, M. A. Alsaiari, M. S. Akhtar, M. Qamar and S. Baskoutas, *Electrochim. Acta*, 2021, **389**, 138661.
24 B. Wang, T. Zhu, H. Bin Wu, R. Xu, J. S. Chen and X. W. Lou, *Nanoscale*, 2012, **4**, 2145–2149.
25 L. Li, R. Jiang, W. Chu, H. Cang, H. Chen and J. Yan, *Catal. Sci. Technol.*, 2017, **7**, 1363–1371.
26 O. Knop, K. I. G. Reid, Y. Sutarno and Y. Nakagawa, *Can. J. Chem.*, 1968, **46**, 3463–3476.
27 R. S. Desai, P. S. Patil, U. E. Mote and D. S. Dalavi, *J. Shivaji Univ. Sci. Technol.*, 2024, **50**, 130.
28 A. UmaSudharshini, M. Bououdina, M. Venkateshwarlu, C. Manoharan and P. Dhamodharan, *Surf. Interfaces*, 2020, **19**, 100535.
29 G. S. Jang, S. Ameen, M. S. Akhtar and H. S. Shin, *Ceram. Int.*, 2018, **44**, 588–595.
30 S. A. Makhlouf, Z. H. Bakr, K. I. Aly and M. S. Moustafa, *Superlattices Microstruct.*, 2013, **64**, 107–117.
31 A. Karthikeyan, R. Mariappan, R. Bakkiyaraj and E. Krishnamoorthy, *J. Mater. Sci.:Mater. Electron.*, 2023, **34**, 728.
32 V. G. Hadjiev, *et al.*, *J. Phys. C:Solid State Phys.*, 1998, **21**, 7.
33 P. S. Gaikar, S. T. Navale, V. V. Jadhav, P. V. Shinde, D. P. Dubal, P. R. Arjunwadkar, F. J. Stadler, M. Naushad, A. A. Ghfar and R. S. Mane, *Electrochim. Acta*, 2017, **253**, 151–162.
34 L. Hou, C. Yuan, L. Yang, L. Shen, F. Zhang and X. Zhang, *RSC Adv.*, 2011, **1**, 1521–1526.
35 M. Kang, H. Zhou, P. Wen and N. Zhao, *ACS Appl. Energy Mater.*, 2021, **4**, 1619–1627.
36 Y. Wang, Y. Lei, J. Li, L. Gu, H. Yuan and D. Xiao, *ACS Appl. Mater. Interfaces*, 2014, **6**, 6739–6747.
37 C. Guo, M. Yin, C. Wu, J. Li, C. Sun, C. Jia, T. Li, L. Hou and Y. Wei, *Front. Chem.*, 2018, **6**, 1–10.
38 T. Zhu, J. S. Chen and X. W. Lou, *J. Mater. Chem.*, 2010, **20**, 7015–7020.
39 S. Wang, S. Lai, P. Li, T. Gao, K. Sun, X. Ding, T. Xie, C. Wu, X. Li, Y. Kuang, W. Liu, W. Yang and X. Sun, *J. Power Sources*, 2019, **436**, 226867.
40 D. S. Dalavi, R. S. Desai and P. S. Patil, *J. Mater. Chem. A*, 2022, **10**, 1179–1226.
41 S. Sun, X. Zhao, M. Yang, L. Ma and X. Shen, *Nanomaterials*, 2015, **5**, 2335–2347.
42 N. R. Chodankar, H. D. Pham, A. K. Nanjundan, J. F. S. Fernando, K. Jayaramulu, D. Golberg, Y. K. Han and D. P. Dubal, *Small*, 2020, **16**, 1–35.
43 M. Aghazadeh, *J. Appl. Electrochem.*, 2012, **42**, 89–94.
44 P. M. Kharade, J. V. Thombare, A. R. Babar, R. N. Bulakhe, S. B. Kulkarni and D. J. Salunkhe, *J. Phys. Chem. Solids*, 2018, **120**, 207–2010.
45 B. R. Duan and Q. Cao, *Electrochim. Acta*, 2012, **64**, 154–161.